The HEXNEM3 nodal flux expansion method for the hexagonal geometry in the code DYN3D

Bilodid, Y.; Grundmann, U.; Kliem, S.;

Originally published:

February 2018

Annals of Nuclear Energy 116(2018), 187-194

DOI: https://doi.org/10.1016/j.anucene.2018.02.037

Perma-Link to Publication Repository of HZDR:

https://www.hzdr.de/publications/Publ-26504

The HEXNEM3 nodal flux expansion method for the hexagonal geometry in the code DYN3D

Yuri Bilodid[1], Ulrich Grundmann[2], Soeren Kliem[1]

[1] *Helmholtz-Zentrum Dresden-Rossendorf,*
Bautzner Landstraße 400, 01328 Dresden, Germany
Tel.: +49 351 260 2020
Fax: +49 351 260 3299
y.bilodid@hzdr.de

[2] *Physikalische Berechnungen, Dresden*

Abstract

This paper describes the derivation of the nodal flux expansion method HEXNEM3, its implementation into the nodal diffusion code DYN3D and the corresponding testing versus benchmarks. As in the earlier versions of expansion method HEXNEM1 and HEXNEM2, the neutron flux in a hexagonal node is expanded into superposition of orthogonal polynomials and exponential functions. The main difference of the HEXNEM3 method is the additional use of tangentially weighted exponential functions and the coupling of neighboring nodes by tangentially weighted fluxes and currents on node surfaces.
The HEXNEM3 method was tested in several benchmark problems, including numerical benchmarks with given cross sections set and reference solutions by fine-mesh finite difference diffusion and a real plant benchmark with Monte Carlo reference solution. The test results demonstrate good agreement with reference solutions and improvement of method accuracy in comparison with HEXNEM1 and HEXNEM2.

1. Introduction

The reactor dynamics code DYN3D is used to simulate static and transient behavior of nuclear reactor cores with hexagonal or rectangular fuel assemblies (Rohde et al., 2016, Kliem et al., 2016). The multi-group neutron diffusion is solved utilizing nodal expansion methods specific for geometry discretization type: rectangular (Beckert and Grundmann, 2008), hexagonal (Grundmann and Hollstein, 1999) or trigonal (Duerigen et al., 2013). In the case of hexagonal assemblies, the three-dimensional neutron diffusion equation is divided by transverse integration into a two-dimensional equation in the hexagonal plane and a one-dimensional equation in the axial direction. These two equations are coupled by the transversal leakages (Grundmann, 1999).
Concerning the HEXNEM1 method the two-dimensional flux expansion in the hexagonal node is based on second order polynomials and six exponential functions directed to the six

faces of the hexagon. The nodes are coupled by the face averaged fluxes and currents. The method is sufficiently accurate for the smaller hexagons of the Russian reactor VVER-440. In order to obtain better results for the larger node size of the VVER-1000 reactor, six exponential functions in direction to the corners are additionally used in the HEXNEM2 method. Fluxes and currents of the three hexagons at the corner are coupled with each other. HEXNEM2 shows an improved accuracy against HEXNEM1 results presented in the reference. However, the conditions at the corners are somewhat complicated, especially at the outer boundary. If face averaged assembly discontinuity factors (ADF) of the neutron fluxes are used to improve the nodal results (Smith, 1986), the HEXNEM2 method requires also ADF for the corner points.
Instead of fluxes and currents at the corner points, tangentially weighted fluxes and currents together with tangentially weighted exponential functions were applied in (Christoskov and Petkov, 2013). The face averaged ADF are used for both fluxes and tangentially weighted fluxes. The method shows improved accuracy against HEXNEM2 in some VVER-1000 problems. For these reasons, the method was implemented as the option HEXNEM3 into the DYN3D code. The equations required for the method implementation are derived in this paper. Results obtained with the three methods HEXNEM1, HEXNEM2 and HEXNEM3 are compared with references.

2. The method HEXNEM3

The 2-dimensional steady state equation of the group *g* in a node is given by

$$-D_g \Delta_r \Phi_g(\boldsymbol{r}) + \Sigma_{r,g} \Phi_g(\boldsymbol{r}) = S_g(\boldsymbol{r}) \tag{1}$$

$$S_g(\boldsymbol{r}) = \frac{1}{k_{eff}} \chi_g \sum_{g'=1}^{G} \nu\Sigma_{f,g'} \Phi_{g'}(\boldsymbol{r}) + \sum_{\substack{g'=1 \\ g' \neq g}}^{G} \Sigma_{s,gg'} \Phi_{g'}(\boldsymbol{r}) - L_g(\boldsymbol{r}) \tag{2}$$

with the 2D Laplacian operator Δ_r and $\boldsymbol{r} = (x, y)$

Besides the leakage of the axial direction L_g the standard notation is used. The fluxes of each energy group *g* are expanded by polynomials up to the 2nd order, exponential functions and tangential weighted exponential functions directed to the six faces of the hexagon.

$$\Phi_g(\boldsymbol{r}) = \sum_{k=0}^{5} c_{g,k} h_k^r\left(\frac{x}{a}, \frac{y}{a}\right) + \sum_{k=1}^{6} a_{g,s,k} e^{B_g \boldsymbol{e}_{s,k} \boldsymbol{r}} + \sum_{k=1}^{6} a_{g,m,k} (\boldsymbol{e}_{n,k} \boldsymbol{r}) e^{B_g \boldsymbol{e}_{s,k} \boldsymbol{r}} \tag{3}$$

The variable *a* describes the half of the distance between two parallel sides of the hexagon in Fig. 1. The area of the hexagon F_{hex} and the length of the faces $\bar{s}$ are given by

$$F_{hex} = 2\sqrt{3}a^2 \text{ and } \bar{s} = \frac{2a}{\sqrt{3}}. \tag{4}$$

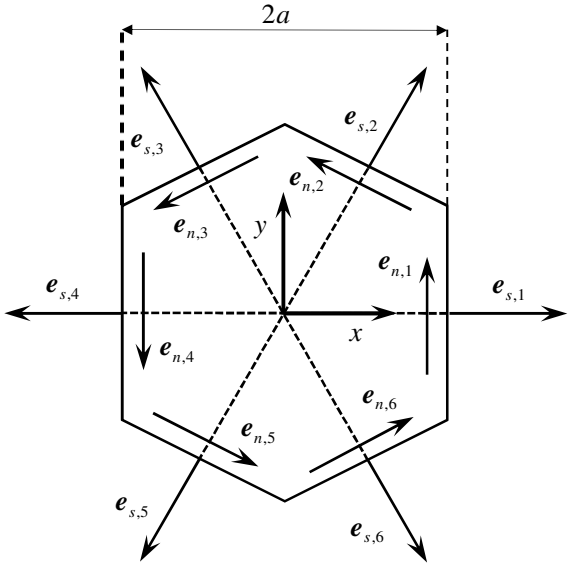

Fig. 1: Hexagon with the vectors of directions $\boldsymbol{e}_{s,k}$ and $\boldsymbol{e}_{n,k}$.

The polynomials $h_k^r(u,v)$

$$h_0^r = \frac{1}{N_0},\ h_1^r(u,v) = \frac{u}{N_1},\ h_2^r(u,v) = \frac{v}{N_2},$$
$$h_3^r(u,v) = \frac{1}{N_3}\left(u^2+v^2-\frac{5}{9}\right),\ h_4^r(u,v) = \frac{1}{N_4}\left(u^2-v^2\right),\ h_5^r(u,v) = \frac{2uv}{N_5} \tag{5}$$

are orthogonal over F_{hex}

$$\iint_{F_{hex}} h_k^r\left(\frac{x}{a},\frac{y}{a}\right) h_l^r\left(\frac{x}{a},\frac{y}{a}\right) dxdy = \delta_{kl}a^2 \tag{6}$$

with Kroneckers symbol δ_{kl}. The normalization factors N_k are given by

$$N_0^2 = 2\sqrt{3},\ N_1^2 = N_2^2 = \frac{5}{9}\sqrt{3},\ N_3^2 = \frac{86}{405}\sqrt{3},\quad N_4^2 = N_5^2 = \frac{56}{135}\sqrt{3}\ . \tag{7}$$

The vectors $\boldsymbol{e}_{s,k}$ and $\boldsymbol{e}_{n,k}$ depend on the basic unit vectors $\boldsymbol{e}_x$ and $\boldsymbol{e}_y$ by

$\boldsymbol{e}_{s,k} = \cos\alpha_k\,\boldsymbol{e}_x + \sin\alpha_k\,\boldsymbol{e}_y$ and $\boldsymbol{e}_{n,k} = -\sin\alpha_k\,\boldsymbol{e}_x + \cos\alpha_k\,\boldsymbol{e}_y$ with $\alpha_k = (k-1)\frac{\pi}{3}$.

The exponential functions and the tangential weighted exponential functions of (3) are solutions of the homogeneous equations (1) with the buckling B_g

$$B_g = \sqrt{\frac{\Sigma_{r,g}}{D_g}} \tag{9}$$

The source of eq. (2) is expanded by the polynomials

$$S_g(x,y) = \sum_{k=0}^{5} s_{g,k} h_k^r\left(\frac{x}{a},\frac{y}{a}\right) \tag{10}$$

Inserting the flux expansion in eq. (1), the following expressions are obtained for the $c_{g,k}$ by the orthogonal conditions (6)

$$c_{g,0} = \frac{s_{g,0}}{\Sigma_{r,g}} + \frac{36}{\left(B_g a\right)^2}\sqrt{\frac{5}{43}}c_{g,3} \tag{11}$$

$$c_{g,k} = \frac{s_{g,k}}{\Sigma_{r,g}} \qquad \text{for} \quad k = 1,2,...,5 \tag{12}$$

The averaged partial currents $J^{\pm}_{g,s,k}$ and the tangential weighted partial currents $J^{\pm}_{g,m,k}$ at the six faces $\bar{s}_k$ are given by

$$J^{\pm}_{g,s,k} = \frac{1}{\bar{s}}\int_{\bar{s}_k}\left[\frac{1}{4}\Phi_g(\boldsymbol{r}) \pm \frac{1}{2}\left[\boldsymbol{e}_{s,k}\boldsymbol{J}_g(\boldsymbol{r})\right]\right]ds\,, \tag{13}$$

$$J^{\pm}_{g,m,k} = \frac{1}{\bar{s}}\int_{\bar{s}_k}\left\{\left(\boldsymbol{e}_{n,k}\boldsymbol{r}\right)\left[\frac{1}{4}\Phi_g(\boldsymbol{r}) \pm \frac{1}{2}\left[\boldsymbol{e}_{s,k}\boldsymbol{J}_g(\boldsymbol{r})\right]\right]\right\}ds \tag{14}$$

$$k = 1,2,....,6\,.$$

with (+) for the outgoing and (-) the incoming values. The currents $\boldsymbol{J}_g(\boldsymbol{r})$ are given by Fick's law

$$\boldsymbol{J}_g(\boldsymbol{r}) = -D_g\nabla\Phi_g(\boldsymbol{r})\,. \tag{15}$$

Inserting the ansatz (3) in (13) and (14), the following equations for the vectors of partial currents $\boldsymbol{J}^{\pm}_{g,s}$ and weighted partial currents $\boldsymbol{J}^{\pm}_{g,m}$ result from the integrations.

$$\boldsymbol{J}^{\pm}_{g,s} = \boldsymbol{P}^{\pm}_{g,s}\boldsymbol{C}_g + \boldsymbol{Q}^{\pm}_{g,ss}\boldsymbol{A}_{g,s} + \boldsymbol{Q}^{\pm}_{g,sm}\boldsymbol{A}_{g,m} \tag{16}$$

$$\boldsymbol{J}^{\pm}_{g,m} = \boldsymbol{P}^{\pm}_{g,m}\boldsymbol{C}_g + \boldsymbol{Q}^{\pm}_{g,ms}\boldsymbol{A}_{g,s} + \boldsymbol{Q}^{\pm}_{g,mm}\boldsymbol{A}_{g,m} \tag{17}$$

$\boldsymbol{C}_g$, $\boldsymbol{A}_{g,s}$, $\boldsymbol{A}_{g,m}$ are the column vectors of the coefficients $c_{g,k}$, $a_{g,s,k}$, $a_{g,m,k}$. The matrices $\boldsymbol{P}, \boldsymbol{Q}$ resulting from the integrations have symmetries similar to the matrices of the HEXNEM2 method (see appendix A).

One has 12 conditions for eliminating the vectors of the coefficients $\boldsymbol{A}_{g,s}$, $\boldsymbol{A}_{g,s}$ from the incoming values $\boldsymbol{J}^{-}_{g,s}$,$\boldsymbol{J}^{-}_{g,m}$ given by the interface conditions to the neighbouring hexagons or the outer boundary conditions. Then the outgoing variables of partial currents $\boldsymbol{J}^{+}_{g,s}$ and tangentially weighted partial currents $\boldsymbol{J}^{+}_{g,m}$ can be represented by the incoming values $\boldsymbol{J}^{-}_{g,s}$, $\boldsymbol{J}^{-}_{g,m}$ and the $\boldsymbol{C}_g$ by using algebraic operations (see Appendix A):

$$\boldsymbol{J}^{+}_{g,s} = \boldsymbol{V}_{g,s}\boldsymbol{C}_g + \boldsymbol{W}_{g,ss}\boldsymbol{J}^{-}_{g,s} - \boldsymbol{W}_{g,sm}\boldsymbol{J}^{-}_{g,m} \tag{18}$$

$$\boldsymbol{J}^{+}_{g,m} = \boldsymbol{V}_{g,m}\boldsymbol{C}_g + \boldsymbol{W}_{g,ms}\boldsymbol{J}^{-}_{g,s} - \boldsymbol{W}_{g,mm}\boldsymbol{J}^{-}_{g,m} \tag{19}$$

An outer and inner iteration scheme is used for the calculation of neutron fluxes in DYN3D. Starting with the first energy group the coefficients of polynomials $\boldsymbol{C}_g$ are calculated from the

polynomial coefficients of the fission source, axial leakage and up-scattering term of the last outer iteration by (11) and (12). Then the outgoing partial currents and the tangential weighted outgoing partial currents of radial direction are calculated from the incoming values by eq. (18) and (19). The one-dimensional equation of the axial direction is treated by a similar nodal method, which is used also with the HEXNEM1 and HEXNEM2 method of the radial direction (Grundmann, 1999). Averaged fluxes and currents are used only for the coupling the nodes in the axial direction.

The incoming values are obtained from the outgoing values of neighbored nodes or boundary conditions. Flux continuity or discontinuity conditions given by ADF can be taken into account. The ADF are used for both fluxes and tangential weighted fluxes. Few inner iterations (3 - 10) are performed for each group. After the last inner iteration, the polynomial coefficients of flux are updated by weighting the flux expansion (3) with the polynomials and integrating over the area of the hexagonal node. The updated coefficients $c^*_{g,k}$ are obtained from

$$\boldsymbol{C}^*_g = \boldsymbol{C}_g + \boldsymbol{I}_{g,s}\boldsymbol{A}_{g,s} + \boldsymbol{I}_{g,m}\boldsymbol{A}_{g,m}\,. \tag{20}$$

Replacing the $\boldsymbol{A}_{g,s}, \boldsymbol{A}_{g,m}$ by the incoming partial currents the equations

$$\boldsymbol{C}^*_g = \boldsymbol{M}^r_g\boldsymbol{C}_g + \boldsymbol{H}^r_{g,s}\boldsymbol{J}^-_{g,s} + \boldsymbol{H}^r_{g,m}\boldsymbol{J}^-_{g,m} \quad . \tag{21}$$

are obtained (see Appendix B). Similar relations exist for the axial problem. The inner iteration of the next energy groups follows with the down scattering terms from the previous groups. If the inner iterations are finished for all energy groups, the new fission rate is calculated and the eigenvalue k_{eff} is evaluated from the fission rates of two successive outer iterations. Convergency of the fission rates terminates the outer iteration accelerated by Chebychev extrapolation.

The node averaged values of neutron fluxes $\overline{\Phi}_g$ are an important result. In contrast to the described scheme the three-dimensional diffusion equation integrated over the node volume

$$\frac{1}{a_z}\left(J^+_{g,+z} - J^-_{g,+z} + J^+_{g,-z} - J^-_{g,-z}\right) + \frac{1}{3a}\sum_{k=1}^{6}\left(J^+_{g,s,k} - J^-_{g,s,k}\right) + \Sigma_{r,g}\overline{\Phi}_g = \overline{S}_g \tag{22}$$

$$\overline{S}_g(\boldsymbol{r}) = \frac{1}{k_{eff}}\chi_g\sum_{g'=1}^{G}\nu\Sigma_{f,g'}\overline{\Phi}_{g'}(\boldsymbol{r}) + \sum_{\substack{g'=1\\ g'\neq g}}^{G}\Sigma_{s,gg'}\overline{\Phi}_{g'}(\boldsymbol{r}) \tag{23}$$

is included in the inner iteration. $J^{\pm}_{g,+z}$, $J^{\pm}_{g,-z}$ are the partial currents at the upper and lower face of the node. The outgoing partial currents are replaced by using eq. (18) and the relevant relations of the axial direction by the incoming values. Based on the symmetry of the matrix $\boldsymbol{W}_{g,sm}$ the tangential weighted incoming partial currents do not occur. Caused by the structure of the matrix $\boldsymbol{V}_{g,s}$ the elements $c_{g,0}$ and $c_{g,3}$ of the vector $\boldsymbol{C}_g$ only contribute to the sum of outgoing partial currents. In analogous way the polynomial coefficients $c^z_{g,0}$ and $c^z_{g,2}$ of axial direction occur in the sum of outgoing partial currents $\left(J^+_{g,+z} + J^+_{g,-z}\right)$. Then the elements $c_{g,0}$, $c_{g,3}, c^z_{g,0}$ and $c^z_{g,2}$ appear in (22) together with the incoming partial currents. Besides a factor

$1/N_0$ the left side of the first of equations (21) describes the averaged flux $\overline{\Phi}_g$ calculated from the ansatz (3). Based on the properties of matrices $\boldsymbol{M}_g^r$, $\boldsymbol{H}_{g,s}^r$ and $\boldsymbol{H}_{g,m}^r$ a linear relation between $\overline{\Phi}_g$, $c_{g,0}$ and $c_{g,3}$ and the sum of the incoming partial currents $J_{g,s,k}^-$ is obtained.

$$c_{g,0} = \kappa_{g,0}\overline{\Phi}_g + \kappa_{g,3}c_{g,3} - \mu_g \sum_{k=1}^{6} J_{g,s,k}^- \tag{24}$$

The constants $\kappa_{g,0}, \kappa_{g,3}, \mu_g$ follow from the described algebraic operations. Then the coefficient $c_{g,0}$ is eliminated in the integral balance equation (22) with the help of (24). It is done in a similar way with the coefficient $c_{g,0}^z$ of axial direction. Finally the integral balance equation is a linear relation between the variables $\overline{\Phi}_g, c_{g,3}, c_{g,2}^z$, the source $\overline{S}_g$ and the incoming partial currents of the node faces

$$\overline{\Phi}_g = \left(\Sigma_{r,g} + \vartheta_g^r + \vartheta_g^z\right)^{-1}\left[\overline{S}_g - \xi_{g,3}^r c_{g,3} - \xi_{g,z}^z c_{g,2}^z + \eta_g^z \sum_{k=1}^{6} J_{g,s,k}^- + \eta_g^r\left(J_{g,+z}^- + J_{g,-z}^-\right)\right] \tag{25}$$

with the constants $\vartheta_g^r, \vartheta_g^z, \xi_{g,3}^r, \xi_{g,2}^z, \eta_g^z, \eta_g^r$ from the algebraic operations. It is used for the calculation of the averaged fluxes $\overline{\Phi}_g$ in each inner iteration step. The arrays of the coefficients $c_{g,0}, c_{g,0}^z$ are not stored and the first equation of (21), the relation (11) and the analogous equations of the axial direction are not needed. During each inner iteration $c_{g,0}$ is calculated for equations (18) and (19) from (24) by using the actual flux values. This modified iteration already applied in HEXNEM1 and HEXNEM2 was stable in numerous problems analyzed with the code DYN3D. The HEXNEM3 method is implemented in the transient part of DYN3D with the equal techniques used also with the HEXNEM1 and HEXNEM2 methods.

3. Results

A set of benchmark problems was solved to verify and validate the proposed HEXNEM3 method and its implementation into the code DYN3D.

1.1. AER-FCM101 numerical benchmark

The AER-FCM101 numerical benchmark is published in the AER benchmark book ("AER benchmark book," 2017). This benchmark represents 1/12 sector of a 3D VVER-1000 prototype reactor core. The benchmark problem contains five types of fuel assemblies, burnable absorber, half-inserted control rods cluster as well as axial and radial reflectors. The homogeneous two-group macroscopic cross-sections and diffusion coefficients for fuel and reflector materials are provided in the benchmark definition. No discontinuity factors are defined. The reference solution was obtained by the CRONOS code (Lautard et al., 1992), utilizing finite elements method and extrapolated to zero mesh size.
The Fig. 2 compares DYN3D results utilizing HEXNEM3 with the benchmark reference solution. Difference in multiplication factor is 7 pcm, maximum difference in relative

assembly power, defined as $100 \cdot \max|\Delta P|$, is 0.4 % and the root mean square deviation (RMS), defined as $100 \cdot \sqrt{\frac{1}{N}\sum^{N} \Delta P^2}$, is 0.2 %.

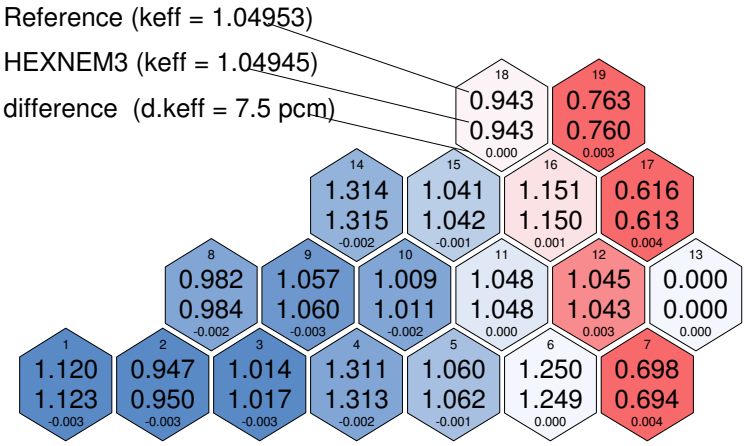

Fig. 2. Assembly power comparison for the three-dimensional AER-FCM101 numerical benchmark.

For the comparison of the reference 3D power distribution in ten axial layers with DYN3D result, the maximum deviation in relative nodal power is 1.3 % and the RMS is 0.6 %. In comparison to ref. (Christoskov and Petkov, 2013) the converged solution is used. If the weaker convergence criteria published there is applied, the maximum deviations are equal to the published values. The HEXNEM3 accuracy is compared with HEXNEM1 and HEXNEM2 in *Table 1*. The HEXNEM2 method accuracy demonstrates significant improvement over HEXNEM1, while HEXNEM3 improve results even more.

Table 1. Deviations of DYN3D results from the reference values.

Method	k_{eff}, pcm	$\Delta P_{assembly}$, %		ΔP_{node}, %	
		max	RMS	max	RMS
3D AER-FCM101 benchmark					
HEXNEM1	41	2.0	1.3	4.0	1.5
HEXNEM2	13	0.6	0.4	1.7	0.8
HEXNEM3	7	0.4	0.2	1.3	0.6
2D VVER-1000 type problem (albedo = 0.5)					
HEXNEM1	59	3.0	2.0	-	-
HEXNEM2	6	0.9	0.5	-	-
HEXNEM3	9	0.2	0.1	-	-
2D VVER-1000 type problem (albedo = 0.125)					
HEXNEM1	50	2.1	1.3	-	-
HEXNEM2	13	0.4	0.2	-	-
HEXNEM3	9	0.2	0.1	-	-
3D X2 benchmark critical state					
HEXNEM1	172	3.7	2.3	6.1	2.6
HEXNEM2	77	1.2	0.7	2.4	0.9
HEXNEM3	77	1.2	0.7	2.4	0.9
2D X2 benchmark rodded state					
HEXNEM1	201	3.7	2.3	-	-
HEXNEM2	87	1.4	0.7	-	-
HEXNEM3	87	1.4	0.7	-	-

1.2. Two-dimensional VVER-1000 type problem

The two-dimensional VVER-1000 type numerical benchmark was described in (Chao and Shatilla, 1995) and used in (Grundmann and Hollstein, 1999) for the verification of the HEXNEM2 method. The benchmark describes 1/6 of a 2D reactor core with homogenous hexagonal fuel assemblies; 25 fuel assemblies are rodded. The boundary conditions are defined by albedo coefficients, two cases are considered: with albedo = 0.5 and 0.125. The two-group macroscopic cross-sections and diffusion coefficients for all materials are provided in the benchmark definition. No discontinuity factors are defined. The reference solutions were obtained by the DIF3D-FD code utilizing fine-mesh finite difference method. Results were extrapolated from DIF3D-FD runs with 486 and 864 triangle/hexagon subdivisions.

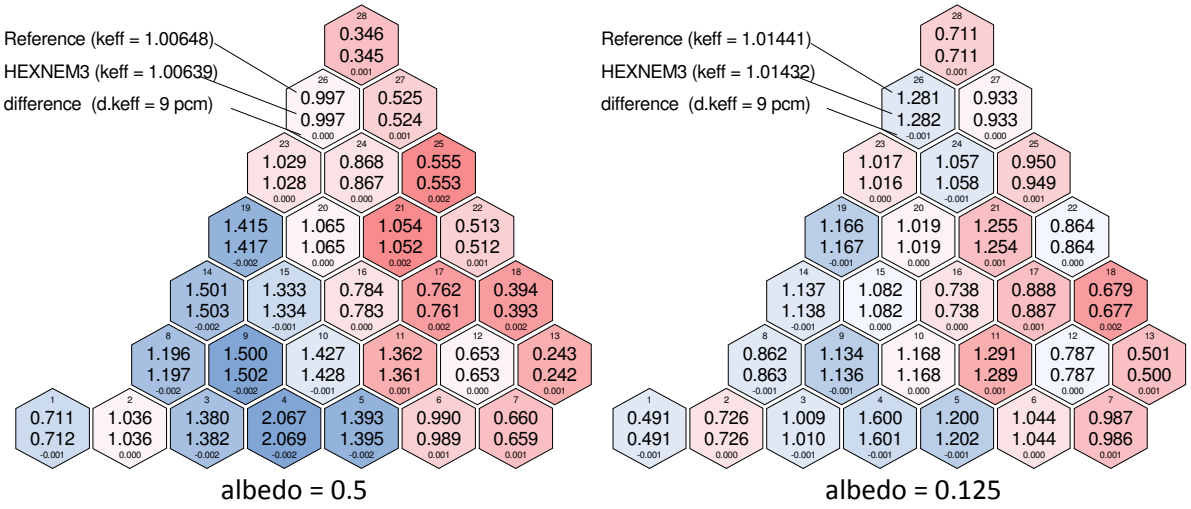

Fig. 3. Assembly power comparison for the 2D VVER-1000 type problem.

Fig. 3 compares DYN3D HEXNEM3 with the benchmark reference solution. For the case albedo = 0.5 the difference in multiplication factor is 9 pcm, maximum difference in relative assembly power is 0.23 % and the root mean square deviation (RMS) is 0.13 %, while for the case albedo = 0.125 the difference in multiplication factor is also 9 pcm, the maximum difference in relative assembly power is 0.18 % and the root mean square deviation (RMS) is 0.08 %. The HEXNEM3 accuracy is compared with HEXNEM1 and HEXNEM2 in *Table 1*. As in the previous case, HEXNEM3 is closer to the reference than HEXNEM2, which in turn is more accurate than HEXNEM1.

1.3. X2 VVER-1000 benchmark

The X2 VVER-1000 benchmark, published in the AER conference proceedings (Lötsch et al., 2009, 2010), describes first 4 fuel cycles of the Khmelnitsky NPP 2nd unit with VVER-1000 reactor. The benchmark specifications contain description of the reactor core material, geometry and operational history supplemented by measured operational data, startup experiments as well as some operational transients.

In this work, DYN3D result for the 1st fuel cycle fresh core hot zero power (HZP) state is compared with Monte Carlo reference. The reference solution is obtained using the Serpent-2 Monte Carlo code (Leppänen et al., 2015) with ENDF/B-VII.0 isotopic library. The Serpent 3D model of the VVER-1000 core features a detailed representation of the fuel assemblies, control rods, and the reflector. The detailed model description and verification was published in (Bilodid and Fridman, 2017). Table 2 demonstrates the very good agreement of Serpent results with the measured values.

Table 2. Comparison of Serpent vs measurements

Parameter	Measurement	Serpent
Multiplication factor k_{eff}	1.0	1.00062±0.8e-5
Temperature reactivity coefficient, pcm/K	-5.39±0.54	-5.67±0.2
Full SCRAM worth, %	7.00±0.43	-7.51±0.001

As long as the benchmark does not provide measurements of power distribution in HZP state, the Serpent solution was used as a reference for verification of DYN3D results. The assembly-wise power distribution was calculated in twenty axial layers. Since the fission source convergence might be an issue in full core simulation, the results of ten independent Serpent runs, each simulating $6*10^9$ neutron histories, were averaged. Additionally, while the problem is 60°-symmetric, Serpent power of symmetrically located assemblies was averaged too. The resulting standard deviation of an assembly relative power is 0.1% while the standard deviation in assembly's axial layer is 0.25%.

The two-group homogenized macroscopic cross sections (XS) for DYN3D were calculated using Serpent. A single assembly model with periodic boundary conditions was used to obtain fuel XS, while reflector XS are obtained from a ¼ core model. The radial reflector discontinuity factors are corrected with ADF of neighboring fuel (Smith, 2017). Axial reflector XS were obtained from a 3D fuel assembly model with periodic radial and black axial boundary conditions.

The DYN3D core model includes two rows of radial reflector and one axial reflector layer under and above a core. Assembly discontinuity factors were applied in DYN3D in radial direction.

Fig. 4 shows the comparison of Serpent and DYN3D results for the 3D critical state problem. Although both DYN3D and Serpent calculations were performed in full 360 degree geometry, the results are 60 degree symmetric and therefore shown in 60 degree sector. The difference in k_{eff} between DYN3D and Serpent is 77 pcm. The maximum error in assembly power is 1.2 %, the RMS is 0.7 %.

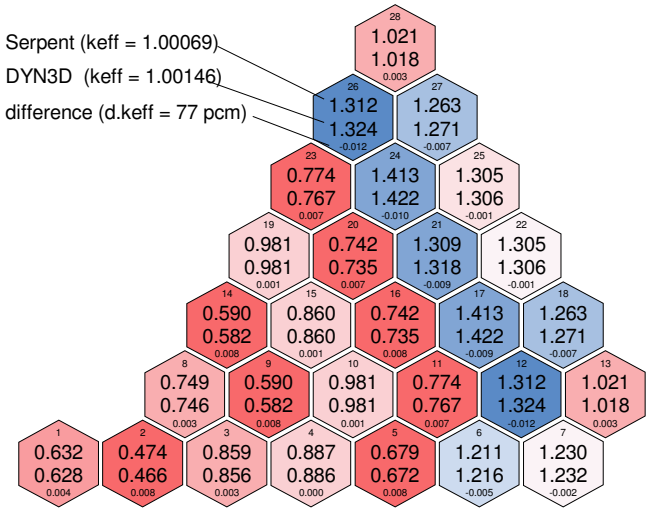

Fig. 4. Assembly power comparison for the three-dimensional X2 HZP critical state.

The comparison of axial power distributions in 20 axial layers obtained by DYN3D and Serpent is illustrated in Fig. 5. The maximum error in a node (assembly layer) power is 2.4 % and the RMS is 0.9 %.

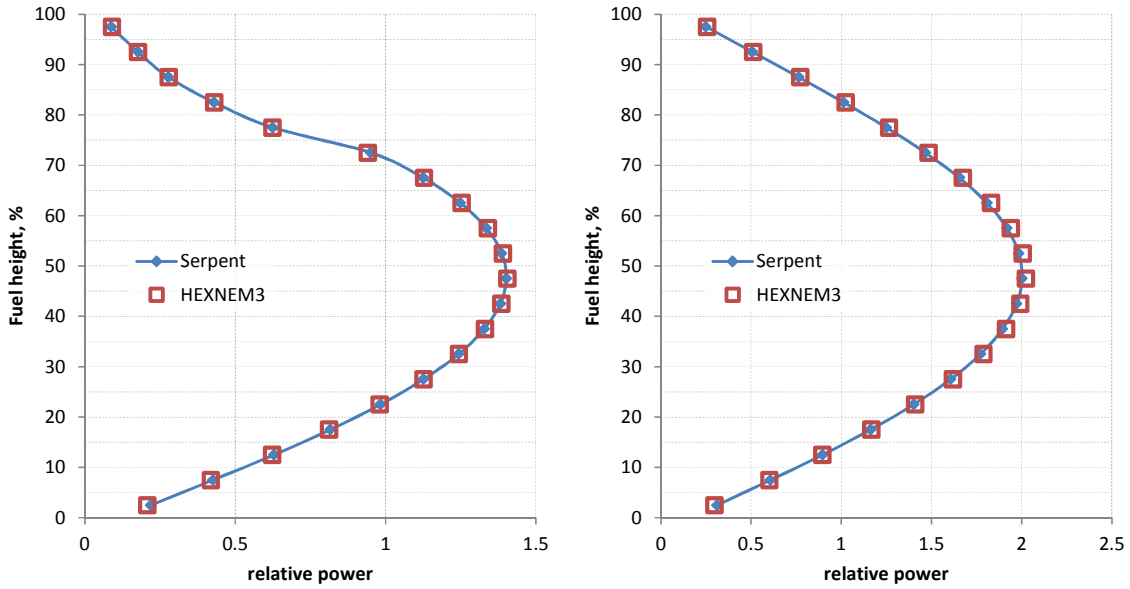

Fig. 5. Axial power distribution in assemblies #15 and #12.

An additional 2D case with inserted control rods was calculated: the same radial geometry and materials as in the previous 3D case, but only one core layer in reflective axial boundary conditions is modeled. The fuel assembly #15 contains control rod absorbers. Fig. 6 (left) demonstrates the comparison of relative power distributions calculated by Serpent and DYN3D.

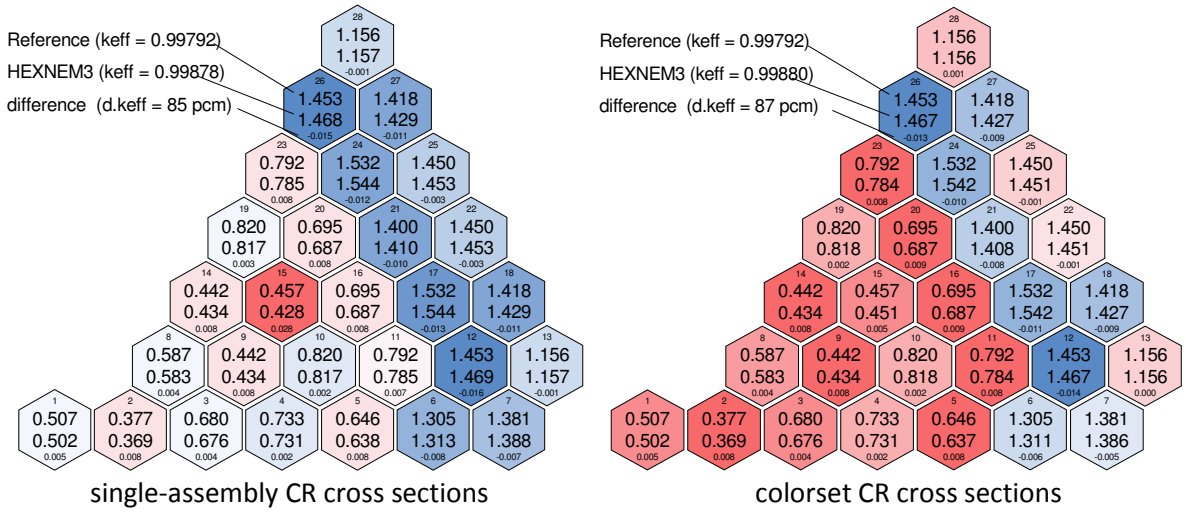

Fig. 6. Assembly power comparison for the two-dimensional rodded case.

The relative power error in the rodded assembly #15 is 2.8 %, which is significantly higher than in unrodded assemblies. This error might be caused by XS generation approach – the XS for rodded assemblies, as well as for unrodded, were produced in single assembly model in periodic boundaries. To prove this point, the second set of XS for the rodded assembly was produced in a colorset model with periodic boundaries, where the rodded assembly is surrounded by unrodded (see Fig. 7). The XS of other materials were kept identical to the in previous case. The DYN3D results using colorset-generated rodded XS are shown in Fig. 6 (right). The relative power error in the rodded assembly #15 decreases to 0.5 %, and the error distribution and magnitude are very similar to the 3D case in Fig. 4.

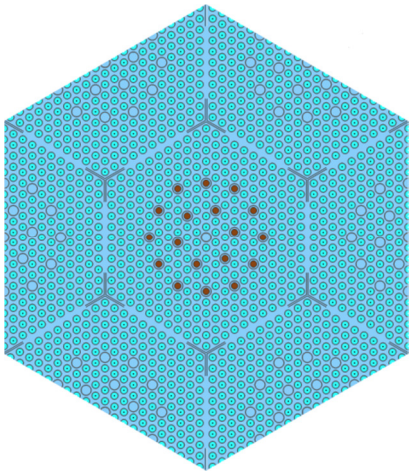

Fig. 7. Colorset model for a control rod.

Results for the 3D and 2D cases obtained by the three HEXNEM methods are compared with Serpent reference solution in *Table 1*. HEXNEM2 and HEXNEM3 results are practically identical, demonstrating very good agreement with the reference, while HEXNEM1 results are significantly worse. Average errors by all three methods for the X2 benchmark cases are notably higher than those in numerical benchmarks since they also include errors of homogenization, energy discretization and diffusion approximation. As it was demonstrated in 2D case with different control rod cross sections (see Fig. 6), DYN3D results could be further improved by more sophisticated homogenization technics. This is simiar to the findings in XS creation procedure and application for fast reactor cores using the SERPENT-DYN3D code chain (Nikitin et al., 2015; Nikitin et al., 2017).

1.4. Test cases summary

In all test cases both HEXNEM2 and HEXNEM3 show much more accurate results than HEXNEM1. In numerical benchmarks AER-FCM101 and 2D VVER-1000 type, where the reference solution is obtained by a fine-mesh finite difference diffusion using benchmark-defined cross sections, HEXNEM3 demonstrates notably better accuracy than HEXNEM2. The maximum error in relative assembly power is 0.4% and in nodal power 1.3%, which could be described as perfect agreement with reference. On the other hand, in the X2 benchmark cases HEXNEM3 results are very similar to HEXNEM2. The reference solution of the X2 problem is obtained by the continuous energy Monte Carlo code Serpent-2, so the deviations of HEXNEM2 and HEXNEM3 from reference are dominated by homogenization and energy discretization errors. The maximum error in relative assembly power is 1.2% and in nodal power 2.4%, which is a very good agreement with the reference.

4. Conclusions

The modified intranodal flux expansion method for two-dimensional hexagonal geometry utilizes tangentially weighted fluxes and currents to couple neighboring nodes. The method was implemented into the nodal diffusion code DYN3D under the name HEXNEM3 and tested versus several benchmarks. In all test cases HEXNEM3 results demonstrate improvement over earlier versions of the nodal expansion method HEXNEM1 and HEXNEM2. The calculation time by the HEXNEM3 method is similar or less than by

HEXNEM2. Another advantage of HEXNEM3 over HEXNEM2 is the simpler discontinuity factors and boundary conditions definition, since no corner values are required.
The future work will be implementing and testing pin power reconstruction (Gomez et al., 2014) with the HEXNEM3 method.

References

AER benchmark book [WWW Document], 2017. http://aerbench.kfki.hu/

Beckert, C. and Grundmann, U., 2008. Development and verification of a nodal approach for solving the multigroup SP3 equations, Annals of Nuclear Energy, 35, pp. 75–86

Bilodid, Y. and Fridman, E., 2017. Serpent solution of X2 benchmark: fresh core at HZP conditions. in Proc.: Proceedings of the 27th AER Symposium on VVER Reactor Physics and Reactor Safety, Munich, Germany, October 17 - 20, 2017

Chao, Y.-A., Shatilla, Y.A., 1995. Conformal Mapping and Hexagonal Nodal Methods —II: Implementation in the ANC-H Code. Nuclear Science and Engineering 121, pp. 210–225.

Christoskov, I., Petkov, P.T., 2013. A development of the HEXNEM nodal expansion method. Annals of Nuclear Energy 51, pp. 235–239.

Duerigen, S.; Rohde, U.; Bilodid, Y.; et al., 2013. The reactor dynamics code DYN3D and its trigonal-geometry nodal diffusion model. Kerntechnik 78, pp. 310-318.

Gomez, A.; Sanchez Espinosa, V. H.; Kliem, S.; Gommlich, A., 2014. Implementation of a fast running full core pin power reconstruction method in DYN3D. Nuclear Engineering and Design 274, pp. 86-97.

Grundmann, U., Hollstein, F., 1999. Two-dimensional intranodal flux expansion method for hexagonal geometry. Nuclear Science and Engineering 133, pp. 201–212.

Grundmann U., “HEXNEM – A Nodal Method for the Solution of the Neutron Dif¬fusion Equation in Hexagonal Geometry”, Proceedings of the M&C’99- Conference on Mathematics and Computations in Nuclear Applications, pp. 1086-1095, Madrid, September, 27 – 30, 1999.

Kliem, S.; Bilodid, Y.; Fridman, E.; et al., 2016. The reactor dynamics code DYN3D. Kerntechnik 81, pp. 170-172.

Lautard, J.J., Loubiere, S., Fedon-Magnaud, C., 1992. CRONOS: A modular computational system for neutronic core calculations (IAEA-TECDOC--678).

Leppänen, J., Pusa, M., Viitanen, T., Valtavirta, V., Kaltiaisenaho, T., 2015. The Serpent Monte Carlo code: Status, development and applications in 2013. Annals of Nuclear Energy 82, pp. 142–150.

Lötsch, T., Khalimonchuk, V., Kuchin, A., 2010. Corrections and additions to the proposal of

a benchmark for core burnup calculations for a VVER-1000 reactor., in Proc.: Proceedings of the 20th AER Symposium on VVER Reactor Physics and Reactor Safety, Hanasaari, Espoo, Finland.

Lötsch, T., Khalimonchuk, V., Kuchin, A., 2009. Proposal of a benchmark for core burnup calculations for a VVER-1000 reactor core., in Proc.: Proceedings of the 19th AER Symposium on VVER Reactor Physics and Reactor Safety, St. St. Constantine and Elena Resort, Bulgaria.

Nikitin, E.; Fridman, E.; Mikityuk, K., 2015. Solution of the OECD/NEA neutronic SFR benchmark with Serpent-DYN3D and Serpent-PARCS code systems. Ann. Nucl. Energy 75, pp. 492-497.

Nikitin, E., Fridman, E., Bilodid Y., Kliem, S., 2017. New version of the reactor dynamics code DYN3D for Sodium cooled Fast Reactor analyses. Kerntechnik 82, pp. 284-288.

Rohde, U., Kliem, S., Grundmann, U., Baier, S., Bilodid, Y., Duerigen, S., Fridman, E., Gommlich, A., Grahn, A., Holt, L., Kozmenkov, Y., Mittag, S., 2016. The reactor dynamics code DYN3D – models, validation and applications. Progress in Nuclear Energy 89, pp. 170–190.

Smith, K.S., 2017. Nodal diffusion methods and lattice physics data in LWR analyses: Understanding numerous subtle details. Progress in Nuclear Energy 101, pp. 360–369.

Smith, K.S., 1986. Assembly homogenization techniques for light water reactor analysis. Progress in Nuclear Energy 17, pp. 303–335.

Appendix A

The vectors of the relations (16) and (17) are

$$\boldsymbol{J}^{\pm}_{g,s} = \begin{pmatrix} J^{\pm}_{g,s,1} \\ J^{\pm}_{g,s,2} \\ J^{\pm}_{g,s,3} \\ J^{\pm}_{g,s,4} \\ J^{\pm}_{g,s,5} \\ J^{\pm}_{g,s,6} \end{pmatrix}, \boldsymbol{J}^{\pm}_{g,m} = \begin{pmatrix} J^{\pm}_{g,m,1} \\ J^{\pm}_{g,m,2} \\ J^{\pm}_{g,m,3} \\ J^{\pm}_{g,m,4} \\ J^{\pm}_{g,m,5} \\ J^{\pm}_{g,m,6} \end{pmatrix}, \boldsymbol{C}_{g} = \begin{pmatrix} c_{g,0} \\ c_{g,1} \\ c_{g,2} \\ c_{g,3} \\ c_{g,4} \\ c_{g,5} \end{pmatrix}, \boldsymbol{A}_{g,s} = \begin{pmatrix} a_{g,s,1} \\ a_{g,s,2} \\ a_{g,s,3} \\ a_{g,s,4} \\ a_{g,s,5} \\ a_{g,s,6} \end{pmatrix}, \boldsymbol{A}_{g,m} = \begin{pmatrix} a_{g,m,1} \\ a_{g,m,2} \\ a_{g,m,3} \\ a_{g,m,4} \\ a_{g,m,5} \\ a_{g,m,6} \end{pmatrix} \tag{A1}$$

with the matrices $\boldsymbol{P}^{\pm}_{g,s}$, $\boldsymbol{P}^{\pm}_{g,m}$ consisting of maximum 6 different elements except for the sign and the factor 2. The circulant matrices $\boldsymbol{Q}^{\pm}_{g,ss}$, $\boldsymbol{Q}^{\pm}_{g,sm}$, $\boldsymbol{Q}^{\pm}_{g,ms}$, $\boldsymbol{Q}^{\pm}_{g,mm}$ have 2 or 4 different elements. The matrices $\boldsymbol{P}$, $\boldsymbol{Q}$ have partly equal partly different symmetry as in the HEXNEM2 method described in (Grundmann and Hollstein, 1999).

$$\boldsymbol{P}^{\pm}_{g,s} = \begin{pmatrix} p^{\pm}_{g,s,0} & 2p^{\pm}_{g,s,1} & 0 & p^{\pm}_{g,s,3} & 2p^{\pm}_{g,s,4} & 0 \\ p^{\pm}_{g,s,0} & p^{\pm}_{g,s,1} & p^{\pm}_{g,s,2} & p^{\pm}_{g,s,3} & -p^{\pm}_{g,s,4} & p^{\pm}_{g,s,5} \\ p^{\pm}_{g,s,0} & -p^{\pm}_{g,s,1} & p^{\pm}_{g,s,2} & p^{\pm}_{g,s,3} & -p^{\pm}_{g,s,4} & -p^{\pm}_{g,s,5} \\ p^{\pm}_{g,s,0} & -2p^{\pm}_{g,s,1} & 0 & p^{\pm}_{g,s,3} & 2p^{\pm}_{g,s,4} & 0 \\ p^{\pm}_{g,s,0} & -p^{\pm}_{g,s,1} & -p^{\pm}_{g,s,2} & p^{\pm}_{g,s,3} & -p^{\pm}_{g,s,4} & p^{\pm}_{g,s,5} \\ p^{\pm}_{g,s,0} & p^{\pm}_{g,s,1} & -p^{\pm}_{g,s,2} & p^{\pm}_{g,s,3} & -p^{\pm}_{g,s,4} & -p^{\pm}_{g,s,5} \end{pmatrix} \tag{A2}$$

$$\boldsymbol{P}^{\pm}_{g,m} = \begin{pmatrix} 0 & 0 & 2p^{\pm}_{g,m,2} & 0 & 0 & 2p^{\pm}_{g,m,5} \\ 0 & -p^{\pm}_{g,m,1} & p^{\pm}_{g,m,2} & 0 & -p^{\pm}_{g,m,4} & -p^{\pm}_{g,m,5} \\ 0 & -p^{\pm}_{g,m,1} & -p^{\pm}_{g,m,2} & 0 & p^{\pm}_{g,m,4} & -p^{\pm}_{g,m,5} \\ 0 & 0 & -2p^{\pm}_{g,m,2} & 0 & 0 & 2p^{\pm}_{g,m,5} \\ 0 & p^{\pm}_{g,m,1} & -p^{\pm}_{g,m,2} & 0 & -p^{\pm}_{g,m,4} & -p^{\pm}_{g,m,5} \\ 0 & p^{\pm}_{g,m,1} & p^{\pm}_{g,m,2} & 0 & p^{\pm}_{g,m,4} & -p^{\pm}_{g,m,5} \end{pmatrix} \tag{A3}$$

$$\boldsymbol{Q}^{\pm}_{g,ss} = \begin{pmatrix} q^{\pm}_{g,ss,1} & q^{\pm}_{g,ss,2} & q^{\pm}_{g,ss,3} & q^{\pm}_{g,ss,4} & q^{\pm}_{g,ss,3} & q^{\pm}_{g,ss,2} \\ q^{\pm}_{g,ss,2} & q^{\pm}_{g,ss,1} & q^{\pm}_{g,ss,2} & q^{\pm}_{g,ss,3} & q^{\pm}_{g,ss,4} & q^{\pm}_{g,ss,3} \\ q^{\pm}_{g,ss,3} & q^{\pm}_{g,ss,2} & q^{\pm}_{g,ss,1} & q^{\pm}_{g,ss,2} & q^{\pm}_{g,ss,3} & q^{\pm}_{g,ss,4} \\ q^{\pm}_{g,ss,4} & q^{\pm}_{g,ss,3} & q^{\pm}_{g,ss,2} & q^{\pm}_{g,ss,1} & q^{\pm}_{g,ss,2} & q^{\pm}_{g,ss,3} \\ q^{\pm}_{g,ss,3} & q^{\pm}_{g,ss,4} & q^{\pm}_{g,ss,3} & q^{\pm}_{g,ss,2} & q^{\pm}_{g,ss,1} & q^{\pm}_{g,ss,2} \\ q^{\pm}_{g,ss,2} & q^{\pm}_{g,ss,3} & q^{\pm}_{g,ss,4} & q^{\pm}_{g,ss,3} & q^{\pm}_{g,ss,2} & q^{\pm}_{g,ss,1} \end{pmatrix} \tag{A4}$$

$$\boldsymbol{Q}^{\pm}_{g,sm} = \begin{pmatrix} 0 & q^{\pm}_{g,sm,2} & q^{\pm}_{g,sm,3} & 0 & -q^{\pm}_{g,sm,3} & -q^{\pm}_{g,sm,2} \\ -q^{\pm}_{g,sm,2} & 0 & q^{\pm}_{g,sm,2} & q^{\pm}_{g,sm,3} & 0 & -q^{\pm}_{g,sm,3} \\ -q^{\pm}_{g,sm,3} & -q^{\pm}_{g,sm,2} & 0 & q^{\pm}_{g,sm,2} & q^{\pm}_{g,sm,3} & 0 \\ 0 & -q^{\pm}_{g,sm,3} & -q^{\pm}_{g,sm,2} & 0 & q^{\pm}_{g,sm,2} & q^{\pm}_{g,sm,3} \\ q^{\pm}_{g,sm,3} & 0 & -q^{\pm}_{g,sm,3} & -q^{\pm}_{g,sm,2} & 0 & q^{\pm}_{g,sm,2} \\ q^{\pm}_{g,sm,2} & q^{\pm}_{g,sm,3} & 0 & -q^{\pm}_{g,sm,3} & -q^{\pm}_{g,sm,2} & 0 \end{pmatrix} \tag{A5}$$

The matrices $\boldsymbol{Q}^{\pm}_{g,ss}$ and $\boldsymbol{Q}^{\pm}_{g,mm}$ as well as $\boldsymbol{Q}^{\pm}_{g,sm}$ and $\boldsymbol{Q}^{\pm}_{g,ms}$ are of equal symmetry. The product of $\boldsymbol{Q}^{\pm}_{g,sm}$ and $\boldsymbol{Q}^{\pm}_{g,ms}$ and the product of two matices of type $\boldsymbol{Q}^{\pm}_{g,ss}$ are of type $\boldsymbol{Q}^{\pm}_{g,ss}$.The multiplications of the matrices $\boldsymbol{Q}^{\pm}_{g,ss}$ and $\boldsymbol{Q}^{\pm}_{g,sm}$ are commutative. Therfore algebraic operations can be applied and the vectors $\boldsymbol{A}_{g,s}$, $\boldsymbol{A}_{g,m}$ are obtained by using the eq. (16) and (17) with the incoming partial currents

$$\begin{aligned} \boldsymbol{A}_{g,s} &= \boldsymbol{R}^{-1}\left(\boldsymbol{Q}^{-}_{g,mm}\boldsymbol{J}^{-}_{g,s} - \boldsymbol{Q}^{-}_{g,sm}\boldsymbol{J}^{-}_{g,m} - \left[\boldsymbol{Q}^{-}_{g,mm}\boldsymbol{P}^{-}_{g,s} - \boldsymbol{Q}^{-}_{g,sm}\boldsymbol{P}^{-}_{g,m}\right]\boldsymbol{C}_{g}\right) \\ \boldsymbol{A}_{g,m} &= \boldsymbol{R}^{-1}\left(-\boldsymbol{Q}^{-}_{g,ms}\boldsymbol{J}^{-}_{g,s} + \boldsymbol{Q}^{-}_{g,ss}\boldsymbol{J}^{-}_{g,m} + \left[\boldsymbol{Q}^{-}_{g,ms}\boldsymbol{P}^{-}_{g,s} - \boldsymbol{Q}^{-}_{g,ss}\boldsymbol{P}^{-}_{g,m}\right]\boldsymbol{C}_{g}\right) \end{aligned} \tag{A6}$$

Die Matrix $\boldsymbol{R}^{-1}$ is the inverse matrix of $\boldsymbol{R}$.

$$\boldsymbol{R} = \left(\boldsymbol{Q}^{-}_{g,ss}\boldsymbol{Q}^{-}_{g,mm} - \boldsymbol{Q}^{-}_{g,sm}\boldsymbol{Q}^{-}_{g,ms}\right) \tag{A7}$$

$\boldsymbol{R}$ and the inverse $\boldsymbol{R}^{-1}$ are of the type $\boldsymbol{Q}^{\pm}_{g,ss}$ with 4 different elements given by

$$\begin{aligned} r_1 &= q^{-}_{g,ss,1}q^{-}_{g,mm,1} + 2q^{-}_{g,ss,2}q^{-}_{g,mm,2} + 2q^{-}_{g,ss,3}q^{-}_{g,mm,3} + q^{-}_{g,ss,4}q^{-}_{g,mm,4} \\ &\quad + 2\left(q^{-}_{g,sm,2}q^{-}_{g,ms,2} + q^{-}_{g,sm,3}q^{-}_{g,ms,3}\right) \\ r_2 &= q^{-}_{g,ss,1}q^{-}_{g,mm,2} + q^{-}_{g,ss,2}\left(q^{-}_{g,mm,1} + q^{-}_{g,mm,3}\right) + q^{-}_{g,ss,3}\left(q^{-}_{g,mm,2} + q^{-}_{g,mm,4}\right) + q^{-}_{g,ss,4}q^{-}_{g,mm,3} \\ &\quad + q^{-}_{g,sm,2}\cdot q^{-}_{g,ms,3} + q^{-}_{g,sm,3}\cdot q^{-}_{g,ms,2} \\ r_3 &= q^{-}_{g,ss,1}q^{-}_{g,mm,3} + q^{-}_{g,ss,2}\left(q^{-}_{g,mm,2} + q^{-}_{g,mm,4}\right) + q^{-}_{g,ss,3}\left(q^{-}_{g,mm,1} + q^{-}_{g,mm,3}\right) + q^{-}_{g,ss,4}q^{-}_{g,mm,2} \\ &\quad - \left(q^{-}_{g,sm,2}\cdot q^{-}_{g,ms,2} + q^{-}_{g,sm,3}\cdot q^{-}_{g,ms,3}\right) \\ r_4 &= q^{-}_{g,ss,1}q^{-}_{g,mm,4} + 2q^{-}_{g,ss,2}q^{-}_{g,mm,3} + 2q^{-}_{g,ss,3}q^{-}_{g,mm,2} + q^{-}_{g,ss,4}q^{-}_{g,mm,1} \\ &\quad - 2\left(q^{-}_{g,sm,2}q^{-}_{g,ms,3} + q^{-}_{g,sm,3}q^{-}_{g,ms,2}\right) \end{aligned} \tag{A8}$$

The 4 elements r_k^{-1} of the inverse matrix $\boldsymbol{R}^{-1}$ are obtained by algebraic operations or using a computer algebra system. With the results of (A6) the expressions of the outcoming partial currents are given by

$$\boldsymbol{J}^{+}_{g,s} = \boldsymbol{V}_{g,s}\boldsymbol{C}_{g} + \boldsymbol{W}_{g,ss}\boldsymbol{J}^{-}_{g,s} - \boldsymbol{W}_{g,sm}\boldsymbol{J}^{-}_{g,m} \tag{A9}$$

$$\boldsymbol{J}_{g,m}^{+} = \boldsymbol{V}_{g,m}\boldsymbol{C}_g + \boldsymbol{W}_{g,ms}\boldsymbol{J}_{g,s}^{-} - \boldsymbol{W}_{g,mm}\boldsymbol{J}_{g,m}^{-}$$

with

$$\begin{aligned}
\boldsymbol{V}_{g,s} &= \boldsymbol{P}_{g,s}^{+} - \boldsymbol{Q}_{g,ss}^{+}\boldsymbol{R}^{-1}\left(\boldsymbol{Q}_{g,mm}^{-}\boldsymbol{P}_{g,s}^{-} - \boldsymbol{Q}_{g,sm}^{-}\boldsymbol{P}_{g,m}^{-}\right) + \boldsymbol{Q}_{g,sm}^{+}\boldsymbol{R}^{-1}\left(\boldsymbol{Q}_{g,ms}^{-}\boldsymbol{P}_{g,s}^{-} - \boldsymbol{Q}_{g,ss}^{-}\boldsymbol{P}_{g,m}^{-}\right), \\
\boldsymbol{V}_{g,m} &= \boldsymbol{P}_{g,m}^{+} - \boldsymbol{Q}_{g,ms}^{+}\boldsymbol{R}^{-1}\left(\boldsymbol{Q}_{g,mm}^{-}\boldsymbol{P}_{g,s}^{-} - \boldsymbol{Q}_{g,sm}^{-}\boldsymbol{P}_{g,m}^{-}\right) + \boldsymbol{Q}_{g,mm}^{+}\boldsymbol{R}^{-1}\left(\boldsymbol{Q}_{g,ms}^{-}\boldsymbol{P}_{g,s}^{-} - \boldsymbol{Q}_{g,ss}^{-}\boldsymbol{P}_{g,m}^{-}\right)
\end{aligned} \tag{A10}$$

and

$$\begin{aligned}
\boldsymbol{W}_{g,ss} &= \boldsymbol{Q}_{g,ss}^{+}\boldsymbol{R}^{-1}\boldsymbol{Q}_{g,mm}^{-} - \boldsymbol{Q}_{g,sm}^{+}\boldsymbol{R}^{-1}\boldsymbol{Q}_{g,ms}^{-}, & \boldsymbol{W}_{g,sm} &= \boldsymbol{Q}_{g,ss}^{+}\boldsymbol{R}^{-1}\boldsymbol{Q}_{g,sm}^{-} - \boldsymbol{Q}_{g,sm}^{+}\boldsymbol{R}^{-1}\boldsymbol{Q}_{g,ss}^{-} \\
\boldsymbol{W}_{g,ms} &= \boldsymbol{Q}_{g,ms}^{+}\boldsymbol{R}^{-1}\boldsymbol{Q}_{g,mm}^{-} - \boldsymbol{Q}_{g,mm}^{+}\boldsymbol{R}^{-1}\boldsymbol{Q}_{g,ms}^{-}, & \boldsymbol{W}_{g,mm} &= \boldsymbol{Q}_{g,ms}^{+}\boldsymbol{R}^{-1}\boldsymbol{Q}_{g,sm}^{-} - \boldsymbol{Q}_{g,mm}^{+}\boldsymbol{R}^{-1}\boldsymbol{Q}_{g,ss}^{-}
\end{aligned} \tag{A11}$$

Based on the symmetries the matrices $\boldsymbol{V}_{g,s}$ and $\boldsymbol{P}_{g,s}^{\pm}$ as well as $\boldsymbol{V}_{g,m}$ and $\boldsymbol{P}_{g,m}^{\pm}$ are of equal types. The types of $\boldsymbol{W}_{g,ss}, \boldsymbol{W}_{g,mm}$ are equal to $\boldsymbol{Q}_{g,ss}^{\pm}$ and $\boldsymbol{W}_{g,sm}$, $\boldsymbol{W}_{g,ms}$ to $\boldsymbol{Q}_{g,sm}^{\pm}$. The elements are obtained from the algebraic operations of eqs. (A10) and (A11).

Appendix B

Weighting the flux expansion (3) with the polynomials (5) the integration over the hexagons leads the relations for the updated coefficients $c_{g,k}^{*}$

$$\boldsymbol{C}_g^{*} = \boldsymbol{C}_g + \boldsymbol{I}_{g,s}\boldsymbol{A}_{g,s} + \boldsymbol{I}_{g,m}\boldsymbol{A}_{g,m} \ . \tag{B1}$$

The elements of the matrices $\boldsymbol{I}_{g,s}$ and $\boldsymbol{I}_{g,m}$ are results of the integrations

$$\frac{1}{a^2}\iint_{F_{hex}} h_k^r\left(\frac{x}{a},\frac{y}{a}\right)e^{B_g\boldsymbol{e}_{s,k}\boldsymbol{r}}\,dxdy \quad \text{bzw.} \quad \frac{1}{a^2}\iint_{F_{hex}} h_k^r\left(\frac{x}{a},\frac{y}{a}\right)\left(\boldsymbol{e}_{n,k}\boldsymbol{r}\right)e^{B_g\boldsymbol{e}_{s,k}\boldsymbol{r}}\,dxdy \ . \tag{B2}$$

The matrix $\boldsymbol{I}_{g,s}$ is equal to the HEXNEM2 method.

$$\boldsymbol{I}_{g,s} = \begin{pmatrix}
i_{g,s,0} & i_{g,s,0} & i_{g,s,0} & i_{g,s,0} & i_{g,s,0} & i_{g,s,0} \\
2i_{g,s,1} & i_{g,s,1} & -i_{g,s,1} & -2i_{g,s,1} & -i_{g,s,1} & i_{g,s,1} \\
0 & i_{g,s,2} & i_{g,s,2} & 0 & -i_{g,s,2} & -i_{g,s,2} \\
i_{g,s,3} & i_{g,s,3} & i_{g,s,3} & i_{g,s,3} & i_{g,s,3} & i_{g,s,3} \\
2i_{g,s,4} & -i_{g,s,4} & -i_{g,s,4} & 2i_{g,s,4} & -i_{g,s,4} & -i_{g,s,4} \\
0 & i_{g,s,5} & -i_{g,s,5} & 0 & i_{g,s,5} & -i_{g,s,5}
\end{pmatrix} \tag{B3}$$

$$\boldsymbol{I}_{g,m} = \begin{pmatrix} 0 & 0 & 0 & 0 & 0 & 0 \\ 0 & -i_{g,m,1} & -i_{g,m,1} & 0 & i_{g,m,1} & i_{g,m,1} \\ 2i_{g,m,2} & i_{g,m,2} & -i_{g,m,2} & -2i_{g,m,2} & -i_{g,m,2} & i_{g,m,2} \\ 0 & 0 & 0 & 0 & 0 & 0 \\ 0 & -i_{g,m,4} & i_{g,m,4} & 0 & -i_{g,m,4} & i_{g,m,4} \\ 2i_{g,m,5} & -i_{g,m,5} & -i_{g,m,5} & 2i_{g,m,5} & -i_{g,m,5} & -i_{g,m,5} \end{pmatrix} \tag{B4}$$

Replacing the vectors of the coefficients $\boldsymbol{A}_{g,s}, \boldsymbol{A}_{g,m}$ with the help of formulas (A6) by the incoming partial currents $\boldsymbol{J}^{-}_{g,s}$, $\boldsymbol{J}^{-}_{g,m}$ and the old polynomial coefficients $\boldsymbol{C}_g$ eq. (B1) results in

$$\boldsymbol{C}^{*}_{g} = \boldsymbol{M}^{r}_{g}\boldsymbol{C}_{g} + \boldsymbol{H}^{r}_{g,s}\boldsymbol{J}^{-}_{g,s} + \boldsymbol{H}^{r}_{g,m}\boldsymbol{J}^{-}_{g,m} \tag{B5}$$

with

$$\boldsymbol{H}^{r}_{g,s} = \boldsymbol{I}_{g,s}\boldsymbol{R}^{-1}\boldsymbol{Q}^{-}_{g,mm} - \boldsymbol{I}_{g,m}\boldsymbol{R}^{-1}\boldsymbol{Q}^{-}_{g,ms} \tag{B6}$$

$$\boldsymbol{H}^{r}_{g,m} = \boldsymbol{I}_{g,m}\boldsymbol{R}^{-1}\boldsymbol{Q}^{-}_{g,ss} - \boldsymbol{I}_{g,s}\boldsymbol{R}^{-1}\boldsymbol{Q}^{-}_{g,sm}$$

$$\boldsymbol{M}^{r}_{g} = \boldsymbol{E} - \boldsymbol{H}^{r}_{g,s}\boldsymbol{P}^{-}_{g,s} - \boldsymbol{H}^{r}_{g,m}\boldsymbol{P}^{-}_{g,m} \tag{B7}$$

with the identity matrix $\boldsymbol{E}$ .The matrix $\boldsymbol{H}^{r}_{g,s}$ has the same structure as $\boldsymbol{I}_{g,s}$ and the structure of $\boldsymbol{H}^{r}_{g,m}$ is equal to $\boldsymbol{I}_{g,m}$. The matrix $\boldsymbol{M}^{r}_{g}$ has the structure

$$\boldsymbol{M}^{r}_{g} = \begin{pmatrix} m^{r}_{g,0} & 0 & 0 & m^{r}_{g,03} & 0 & 0 \\ 0 & m^{r}_{g,1} & 0 & 0 & 0 & 0 \\ 0 & 0 & m^{r}_{g,2} & 0 & 0 & 0 \\ m^{r}_{g,30} & 0 & 0 & m^{r}_{g,3} & 0 & 0 \\ 0 & 0 & 0 & 0 & m^{r}_{g,4} & 0 \\ 0 & 0 & 0 & 0 & 0 & m^{r}_{g,5} \end{pmatrix} \tag{B8}$$

with only few elements obtained by algebraic operations.